



# Morphology and composition dependence of multicomponent Cu-based nanoreactor for tandem electrocatalysis CO<sub>2</sub> reduction

Wanfeng Xiong<sup>a,b</sup>, Duanhui Si<sup>a,d</sup>, Jundong Yi<sup>a</sup>, Yuanbiao Huang<sup>a,d</sup>, Hongfang Li<sup>a,c,d,\*</sup>,  
Rong Cao<sup>a,b,c,d,\*</sup>

<sup>a</sup> State Key Laboratory Structural Chemistry, Fujian Institute of Research on the Structure of Matter, Chinese Academy of Sciences, Fuzhou 350002, China

<sup>b</sup> College of Chemistry and Chemical Engineering, Xiamen University, Xiamen 361005, China

<sup>c</sup> University of Chinese Academy of Sciences, Beijing 100049, China

<sup>d</sup> Fujian Science & Technology Innovation Laboratory for Optoelectronic Information of China, Fuzhou, Fujian 350108, China

## ARTICLE INFO

### Keywords:

CO<sub>2</sub> electroreduction  
Multicomponent Cu-based catalyst  
Tandem catalysis  
Metal organic frameworks

## ABSTRACT

Multicomponent heterogeneous catalysts present excellent catalytic performance attributed to the synergistic effect of multi-sites. Nevertheless, identifying the composition of the multi-sites and exploring the synergistic catalytic mechanisms for the multiple active sites in electrocatalytic CO<sub>2</sub> reduction reaction (CO<sub>2</sub>RR) still lack intensive study. This work regulates the chemical composition of Cu-based nanoreactors readily by adjusting the geometrical morphology of metal-organic frameworks precursor. The obtained cuboctahedron nanoreactor containing Cu-N<sub>4</sub>/Cu<sub>2</sub>O/Cu multiple active sites exhibits excellent CO<sub>2</sub>RR selectivity towards deep reduction product (80%) with high current density. Moreover, the tandem catalytic mechanism of multicomponent active sites has been studied intensively. The CO<sub>2</sub> molecule is firstly reduced in Cu-N<sub>4</sub> sites to form CO and then the CO is transferred to Cu<sub>2</sub>O/Cu sites for further deep reduction. The high concentration of CO provided by Cu-N<sub>4</sub> sites decreases the free energy of rate-determining step for CH<sub>4</sub> products in Cu<sub>2</sub>O sites. This work provides a promising direction for designing and synthesizing multicomponent Cu-based tandem catalysts to access high efficiency and selectivity in the electrocatalytic CO<sub>2</sub> reduction reaction.

## 1. Introduction

With the development of clean energy such as wind power and hydropower, electricity has become an invariably energy supply method now [1,2]. Catalytic technology relying on electricity has become a focused research in recent years [3–6]. Electrocatalytic CO<sub>2</sub> reduction reaction (CO<sub>2</sub>RR) can effectively convert CO<sub>2</sub> into value-added chemicals or fuels, thereby realizing the carbon cycle and tackling the problems caused by excessive CO<sub>2</sub> emissions [7,8]. Despite there have breakthroughs in catalysts and reaction configuration design recently, the energy efficiency of CO<sub>2</sub>RR cannot fulfill commercial demands [9,10]. Improving the selectivity and productivity of CO<sub>2</sub>RR for deep reduction products (hydrocarbons, alcohols, etc.) are crucial for technological breakthrough.

Copper has been well confirmed as the main metal to convert CO<sub>2</sub> to deep reduction products [11]. However, conventional Cu-based electrodes usually result in poor selectivity with wide range products

because of the similar binding energy for different CO<sub>2</sub> reduction intermediates [12]. Recently, considerable efforts have been devoted to enhance the selectivity of copper-based catalysts, including forming Cu alloys with other metals [13], doping Cu with heteroatoms [14,15], controlling the crystal plane and creating mixture valence states of Cu [16,17]. Nevertheless, it is inevitable to add extra carbon support to promote charge transfer and maximize the utilization of active sites in these works. However, the introduction of support may affect the electronic structure of Cu-based nanoparticles (NPs) and thus mislead the judgment of structure-activity relationship [18]. Therefore, it is more attractive to develop self-supported Cu-based catalysts and study their catalytic mechanism in CO<sub>2</sub>RR process.

Metal-organic frameworks (MOFs) are porous crystalline materials assembled with metal nodes and organic linkers [19–23]. The structural feature makes them ideal precursors to prepare carbon supported metal catalysts. It is well known that the nanomaterials derived from MOFs generally contained multicomponent active sites, including multivalent

\* Corresponding authors at: State Key Laboratory Structural Chemistry, Fujian Institute of Research on the Structure of Matter, Chinese Academy of Sciences, Fuzhou 350002, China.

E-mail addresses: [hongfangli@fjirsm.ac.cn](mailto:hongfangli@fjirsm.ac.cn) (H. Li), [rcao@fjirsm.ac.cn](mailto:rcao@fjirsm.ac.cn) (R. Cao).

<https://doi.org/10.1016/j.apcatb.2022.121498>

Received 18 February 2022; Received in revised form 4 May 2022; Accepted 8 May 2022

Available online 11 May 2022

0926-3373/© 2022 Elsevier B.V. All rights reserved.

NPs, metal clusters and single-atom sites, etc [24–30]. All these active sites have been recognized to play different roles in catalytic process. Recently, MOFs-derived CuO/C nanoboxes [31], Cu<sub>x</sub>O/C composites [18], and Cu-N-C materials [32] have been used as catalysts for CO<sub>2</sub>RR. However, the main attention of these works has been paid to explore the changing of Cu-based metal during the catalytic reaction. The complex multicomponent structure of the Cu-based catalysts still lacks systematic study, which hampers the sufficient understanding on catalytic mechanism of the Cu-based materials. Therefore, it is highly desirable to design a multicomponent Cu-based catalyst with identified multiple active sites, excellent performance and definite catalytic mechanism toward CO<sub>2</sub>RR.

In this contribution, we prepared a serial of Cu-based nanoreactors containing Cu-N<sub>4</sub>/Cu<sub>2</sub>O/Cu multiple active sites derived from MOFs precursor. The chemical composition of the Cu-based nanoreactors can be readily controlled by adjusting the geometrical morphology of MOFs precursor. The obtained cuboctahedron-shaped (CHK-cOCTA) nanoreactor had a high content of Cu-N<sub>4</sub>/Cu<sub>2</sub>O active sites and displayed the best catalytic activity toward CO<sub>2</sub>RR. The Faradic efficiency toward deep reduction products was nearly 80% and the CH<sub>4</sub> selectivity was up to 60%. Combined with *in-situ* attenuated total reflection Fourier transform infrared spectra and density functional theory calculation, the detailed catalytic mechanism of the CHK-cOCTA nanoreactor has been established. The enhancement of CO<sub>2</sub>RR was stemmed from the tandem catalytic steps through the Cu-N<sub>4</sub>/Cu<sub>2</sub>O/Cu multicomponent active sites. The CO<sub>2</sub> was firstly reduced to CO in Cu-N<sub>4</sub> sites and then the CO was transferred to Cu<sub>2</sub>O/Cu active sites for further hydrogenating to deep reduction products. The high coverage of CO in Cu<sub>2</sub>O active site reduces the free energy for CH<sub>4</sub> generations, which promoted excellent catalytic selectivity and high current density toward CH<sub>4</sub>.

## 2. Experimental section

### 2.1. Reagents and chemicals

All reagents and chemicals were obtained commercially and used without further purification. CuSO<sub>4</sub> 5 H<sub>2</sub>O, triethylamine (TEA), KNO<sub>3</sub>, NaNO<sub>3</sub> and KBr were purchased from Sinopharm Chemical Reagent Co. Ltd. 1,3,5-Benzenetricarboxylic acid (H<sub>3</sub>BTC) was purchased from Aladdin (Shanghai), China. Deionized (DI) water was from Milli-Q System (Millipore, Billerica, MA).

### 2.2. Synthesis of BTC-TEA salt

The H<sub>3</sub>BTC (2.1 g, 0.01 M) was dissolved in TEA solution (10 mL, 30 wt% in water). After 30 min ultrasonic treatment, the obtained clarified liquid was then concentrated through rotary evaporation and dried at 70 °C under vacuum. The obtained BTC-TEA salt was then dissolved in a mixture solution of ethanol (50 mL) and deionized water (200 mL) for further using.

### 2.3. Synthesis of TEA modified HKUST-1 with different geometry

TEA modified HKUST-1 with different geometry was synthesized following the reported method with some improvements [33]. In the typical experiment, 0.3 mL CuSO<sub>4</sub> aqueous solution (0.1 M) was added in 25 mL mixture solution of ethanol and deionized water (1:1). Then, 0.2 mL prepared BTC-TEA salt solution was added and further reacted for 5 min under ultrasonic treatment. The obtained cyan powder was separated by centrifugation and washed with H<sub>2</sub>O and ethanol three times. After drying at 70 °C overnight, the final cuboctahedron product was noted as HK-cOCTA. The synthetic procedures of HK-CUBE, HK-tOCTA and HK-oOCTA were similar with HK-cOCTA, just adding extra KNO<sub>3</sub> (25.3 mg, 0.01 M), NaNO<sub>3</sub> (42.5 mg, 0.02 M) and KBr (1.49 g, 0.5 M) respectively in the mixture solution of ethanol and deionized water (1:1).

### 2.4. Preparation of Cu-based nanoreactors with different geometry

The Cu-based nanoreactors were prepared by calcination of the TEA modified HKUST-1 with different geometry. Typically, the dry HKUST-1 precursor was transferred to a corundum ark and pyrolyzed in tubed furnace at 310 °C (heating rate 2 °C min<sup>-1</sup>) for 30 min under nitrogen atmosphere. The obtained Cu-based nanoreactors were noted as CHK-cOCTA, CHK-CUBE, CHK-tOCTA and CHK-oOCTA, respectively.

### 2.5. Preparation of CHK-1

The unmodified HKUST-1 was used as precursor to synthesize CHK-1 sample. In a typical method, the CuSO<sub>4</sub> solution was added into H<sub>3</sub>BTC solution by dropwise and reacted for one hour. The obtained HKUST-1 precursor was separated by centrifugation, washed with H<sub>2</sub>O and ethanol three times, dried at 70 °C overnight and following the same calcination process at 310 °C for 30 min under N<sub>2</sub> atmosphere.

### 2.6. Electrocatalytic CO<sub>2</sub> reduction reaction (CO<sub>2</sub>RR) measurements

All of the electrochemical measurements of CO<sub>2</sub>RR were performed in a H-typed cell separated by an proton exchange membrane (Nafion 117) at room temperature. The three-electrode system by using the glassy carbon loaded with the catalyst, Ag/AgCl with saturated KCl solution and Pt mesh was performed in all the measurements. The 35 mL 0.1 M KHCO<sub>3</sub>/0.1 M KCl mixed electrolyte was filled in each cell compartment. In the typical preparation of working electrode, 4 mg of catalyst was dispersed in a mixed solution with 960 μL isopropanol and 40 μL Nafion solution (5 wt%, Adamas). Then it was sonicated for 40 min to form the ink. The 40 μL obtained ink was dropped onto the surface of the glassy carbon electrode (GCE, 0.785 cm<sup>2</sup>) and dried at room temperature, giving a catalyst loading of 204 μg cm<sup>-2</sup>.

Before the measurement, the CO<sub>2</sub> (>99.99%) gas was supplied to the cathode cell for 30 min to make the electrolyte CO<sub>2</sub>-saturated. During the test, the CO<sub>2</sub> was continuously purged with the rate of 30 sccm. All the reported potentials were converted to reversible hydrogen electrode (RHE) by the equation:  $E_{vs. RHE} = E_{vs. Ag/AgCl} + 0.0592 pH + 0.197$ . The cyclic voltammetry scan from 0 to 200 mV (vs. RHE) with the rate of 100 mV s<sup>-1</sup> was first applied to clean the surface of electrode. The LSV curves were proceed in CO<sub>2</sub>-saturated 0.1 M KHCO<sub>3</sub>/0.1 M KCl (pH = 6.8) with the scan rate of 10 mV s<sup>-1</sup>. The CO<sub>2</sub> electroreduction reactions were proceed at different potential by chronoamperometric measurement. Typically, 0.8 mL gas products were detected through gas chromatograph (GC, Agilent, 7820 A) every 30 min. After 1 h reaction, 0.4 mL liquid products were taken and mixed with 0.1 mL DMSO/D<sub>2</sub>O solution (0.5% DMSO content). The liquid solution with DMSO standard was then quantitatively analyzed by NMR (JES-ECZ400S, JEOL).

The gas product Faradic efficiency was calculated by the following equation:

$$FE_{gas} = \frac{P \times v \times f \times 10^{-6} (m^3/mL)}{RT} \times \frac{n_e F}{I \times 60 (s/min)} \quad (1)$$

Where  $P$  is the atmosphere ( $1.013 \times 10^5$  Pa);  $v$  is the gas product concentration measured by GC (in ppm);  $f$  is the gas flow rate (30 (30 sccm));  $n_e$  is the electron transfer number for product formation;  $F$  is the Faraday constant ( $96,485$  C mol<sup>-1</sup>);  $R$  is the universal gas constant ( $8.314$  J mol<sup>-1</sup> K<sup>-1</sup>);  $T$  is the room temperature (298 K);  $I$  is the total steady-state cell current.

The liquid product Faradic efficiency was calculated by the following equation:

$$FE_{liquid} = n_e F \frac{n}{Q} \quad (2)$$

Where  $n_e$  is the electron transfer number for product formation;  $F$  is the Faraday constant ( $96,485$  C mol<sup>-1</sup>);  $n$  is the liquid product content

calculated by NMR result with DMSO as internal standard substance (mol);  $Q$  is the total charge in a period of reaction time (C).

## 2.7. Characterization

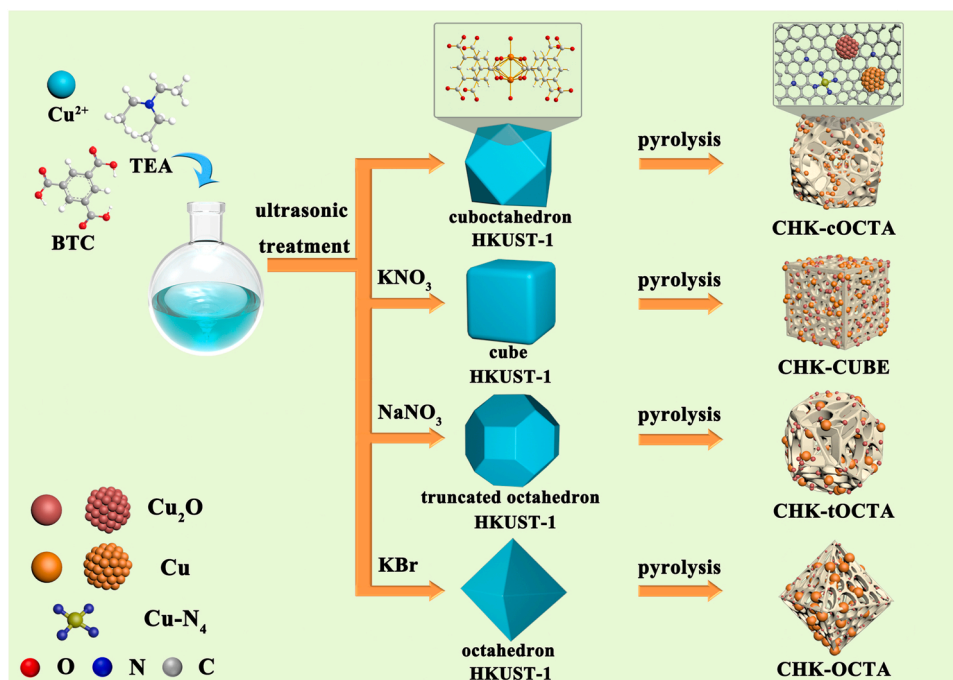
Scanning electron microscopy (SEM) images were photographed on a JSM6700-F (JEOL) SEM working at 10 kV. Transmission electron microscope (TEM), High-angle annular dark-field scanning transmission electron microscopy (HAADF-STEM) and the energy-dispersive X-ray spectroscopy (EDS) images were recorded with Titan Cubed Themis G2 300 (FEI) high-resolution transmission electron microscope working at 200 kV. Powder X-ray diffraction (PXRD) patterns were recorded on a Miniflex 600 X-ray diffractometer (Cu  $K\alpha$ ,  $\lambda = 0.154$  nm). Thermogravimetry analysis (TGA) was conducted with SDT-Q600 (TA Instruments, America). The  $N_2$  adsorption-desorption isotherms were measured using Micromeritics ASAP 2460 instrument and the Brunauer-Emmett-Teller (BET) model was used to evaluated the specific surface areas. The pore distributions were obtained through the calculation from the Barrett-Joyner-Halenda (BJH) adsorption isotherms. The  $CO_2$  adsorption isotherms were acquired by using Micromeritics ASAP 2020 instrument. The  $CO_2$  temperature programmed desorption ( $CO_2$ -TPD) was performed on AutoChem1 II 2920. Without pretreatment with hydrogen reduction, all of the samples adsorbed  $CO_2$  for 1 h (30 mL/min), and then blew 20 min with He. After treatment, the TPD analysis was performed from 10 °C to 700 °C with the 10 °C/min heating rate under  $N_2$  flow. X-ray photoelectron spectroscopy (XPS) measurements were performed on an ESCALAB 250Xi X-ray photoelectron spectrometer (Thermo Fisher) using monochromatized Al  $K\alpha$  radiation (15 kV, 10 mA). The data of XAFS spectra at the Cu L-edge were recorded using total electron yield (TEY) mode at the BL08U in Shanghai Synchrotron Radiation Facility (SSRF), China. The data of XAFS spectra at the Cu K-edge (8979 eV) were collected at the beamline BL14W1 station of the SSRF, China. ATR-FTIR experiments were recorded on a Nicolet6700 (Thermo Fisher) equipped a liquid nitrogen cooled MCT detector.

## 3. Results and discussion

### 3.1. Structural analysis of the catalysts

In the crystal growth process, the supersaturation of solution will affect the chemical potential of crystal and finally influences the crystal's morphologies [34,35]. The crystal's chemical potential will affect the reduction rate of Cu element in the calcination process, which resulted in different chemical composition in the obtained nanoreactors. As shown in Scheme 1, the modified HKUST-1 was firstly constructed with copper nitrate and triethylamine-trimesic acid salt (TEA-BTC) in a mixed solution (ethanol and  $H_2O$ ) at room temperature. The supersaturation of solution was controlled through adding different inorganic salt during the synthetic procedure and a series of HKUST-1 precursors with different morphologies has been prepared. The scanning electronic microscopy (SEM) images (Fig. S1) indicated that the modified HKUST-1 displayed cuboctahedron (HK-cOCTA), cube (HK-CUBE), truncated octahedron (HK-tOCTA) and octahedron (HK-OCTA) shapes with smooth surfaces. The powder X-ray diffraction (PXRD) pattern (Fig. S2a) peaks of as-prepared HKUST-1 matched well with the simulated XRD pattern. In the following calcination process, the HKUST-1 precursors were completely decomposed into Cu-based nanoreactors. The N element derived from TEA was successfully doped into the carbon matrix and the coordinated copper ions were converted to Cu-based active sites including Cu NPs,  $Cu_2O$  NPs and Cu single-atom coordinated with partial doped-N. The calcination temperature was determined from thermogravimetric analysis (TGA) of HKUST-1 in  $N_2$  atmosphere (Fig. S2b) and 310 °C was chosen to ensure complete decomposition of HKUST-1 precursor.

The morphology of the as-prepared Cu-based nanoreactors was investigated by SEM (Fig. 1a-d) and transmission electron microscopy (TEM) (Fig. 1e-h). The Cu-based nanoreactors maintained the same cuboctahedron (CHK-cOCTA), cube (CHK-CUBE), truncated octahedron (CHK-tOCTA) and octahedron (CHK-OCTA) shape as their original HKUST-1 precursor. The surfaces was somewhat wrinkled and rough due to the appearance of graphene layers and pores. The high-angle annular dark-field scanning transmission electron microscopy (HAADF-STEM) images (Fig. 1i-l) demonstrated that the NPs size in



Scheme 1. Illustration of the fabrication of different Cu-based nanoreactors.



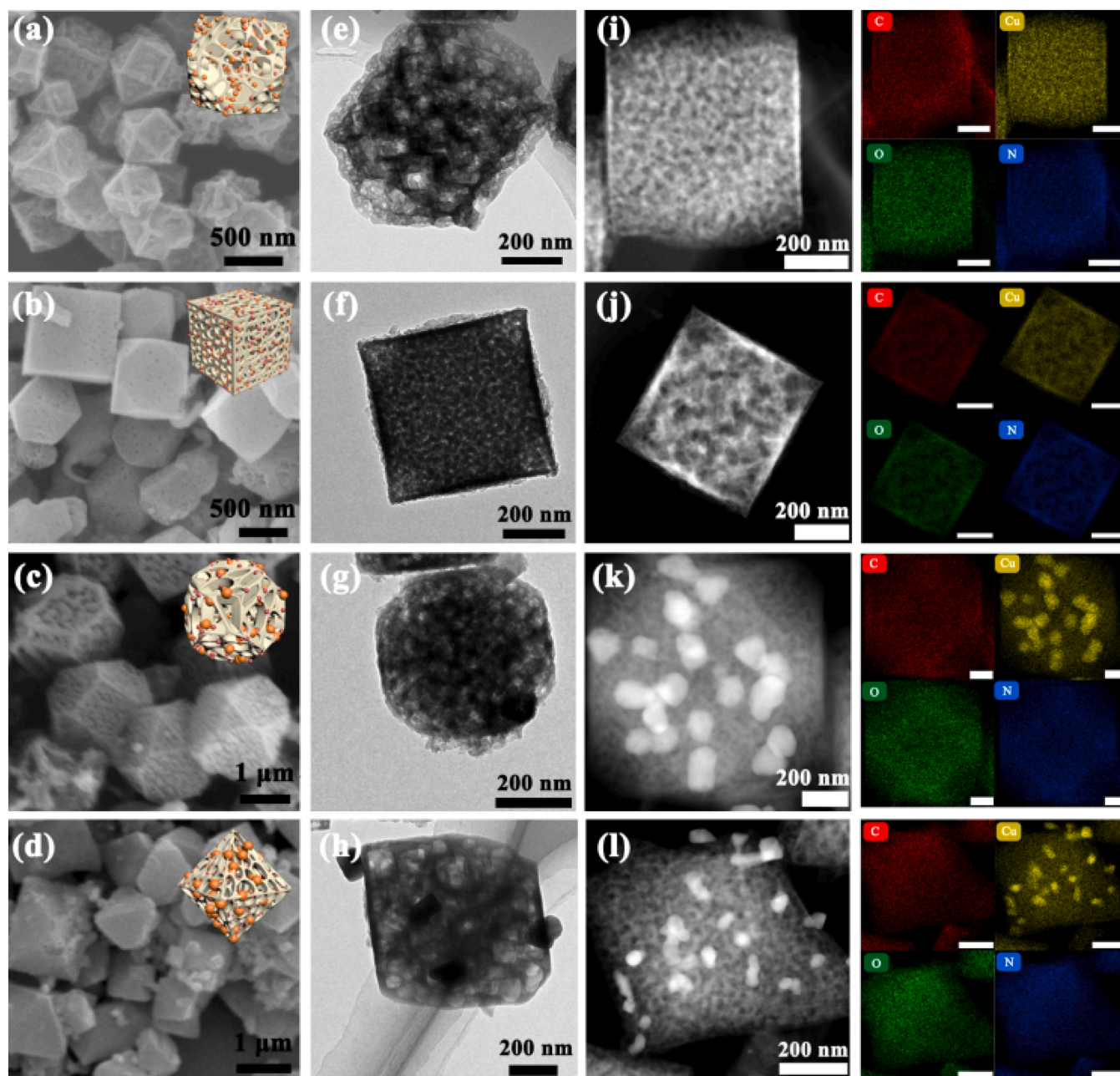


**Fig. 1.** (a-d) SEM, (e-h) TEM, (i-l) HAADF-STEM and EDS mapping images of CHK-cOCTA, CHK-CUBE, CHK-tOCTA and CHK-OCTA (From top to bottom, the scale in the EDS mapping images is 200 nm).

different Cu-based nanoreactors distinguished greatly. No obvious NPs could be observed in CHK-cOCTA and CHK-CUBE, the Cu, C, N and O elements were dispersed homogeneously throughout the frameworks (Fig. 1i and 1j). The size of NPs in CHK-tOCTA (Fig. 1k) and CHK-OCTA (Fig. 1l) increased significantly. The signal of Cu element in the EDS mapping was partly strengthened in the NPs areas. Based on the results of HAADF-STEM and EDS mapping, it could be deduced that the growing NPs were possibly ascribed to Cu NPs. The EDS analysis for the single large particles in CHK-OCTA revealed that the Cu element content was nearly 98% (Fig. S3), which further confirmed the existence of Cu NPs. However, it should not be ignored that the Cu element in the rest region of the nanoreactor distributed uniformly, which is coincided with N and O element. This result indicated that the tiny  $\text{Cu}_2\text{O}$  NPs and  $\text{Cu-N}_x$  single-atom active sites might co-exist in this area. The representative HRTEM images of CHK-cOCTA indicated that the Cu and  $\text{Cu}_2\text{O}$  NPs in such nanoreactor both exhibited (111) lattice planes (Fig. S4). The phase

composition of the Cu-based nanoreactors was further characterized by PXRD pattern (Fig. 2a). The HKUST-1 phase disappeared completely and a mixture of Cu and  $\text{Cu}_2\text{O}$  could be detected. Both Cu and  $\text{Cu}_2\text{O}$  exhibited the (111) plane as the main lattice planes. The intensity of  $\text{Cu}_2\text{O}$  peaks remained nearly same in different samples. However, the intensity of Cu peak increased significantly from CHK-cOCTA to CHK-OCTA, indicating more or larger Cu NPs have been formed. Obviously, the Cu node in HK-tOCTA and HK-OCTA precursor were more easily reduced into larger Cu NPs. Therefore, the chemical composition of the Cu-based nanoreactors could be readily controlled through regulating the geometrical morphology of MOFs precursor.

To gain an insight into the chemical states of the Cu species in the as-prepared Cu-based nanoreactors, X-ray photoelectron spectroscopy (XPS) was conducted firstly. The Cu 2p spectra (Fig. 2b) for all samples revealed the signals of Cu (II) and Cu (0 or I). The intensity of Cu (II) peak showed a significant decrease from CHK-cOCTA to CHK-OCTA due



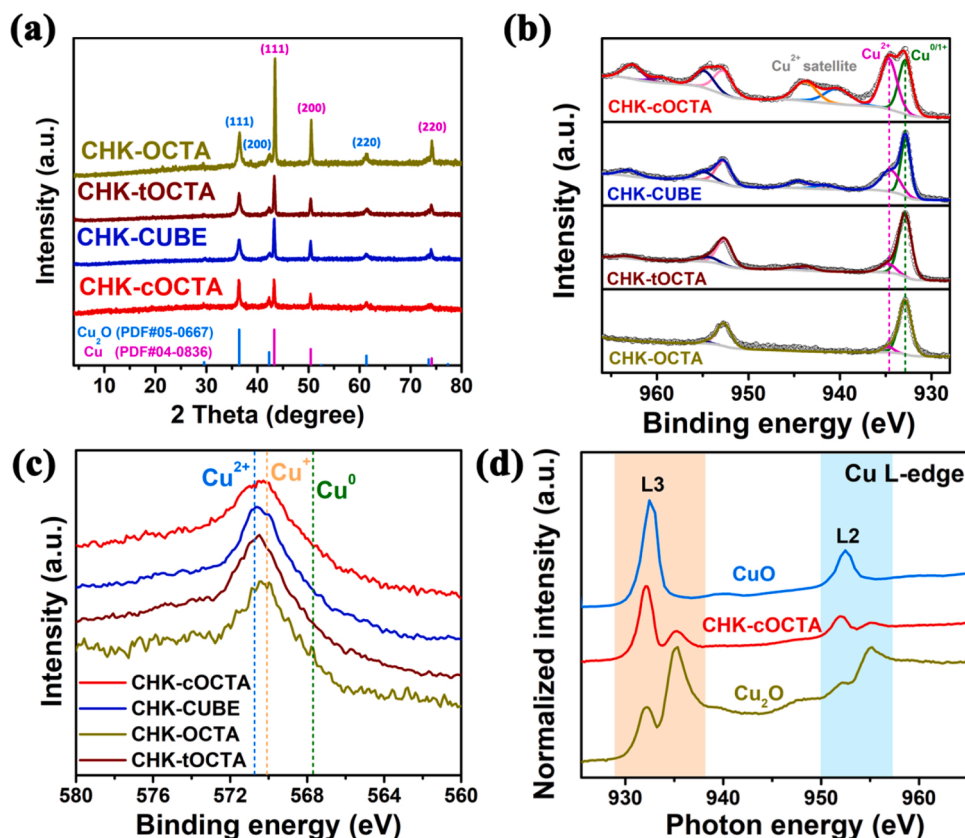


Fig. 2. (a) PXRD pattern (b) XPS Cu 2p spectra and (c) Cu LMM Auger spectra of Cu-based nanoreactors, (d) Cu L-edge XANES spectra of CHK-cOCTA and CuO, Cu<sub>2</sub>O standard.

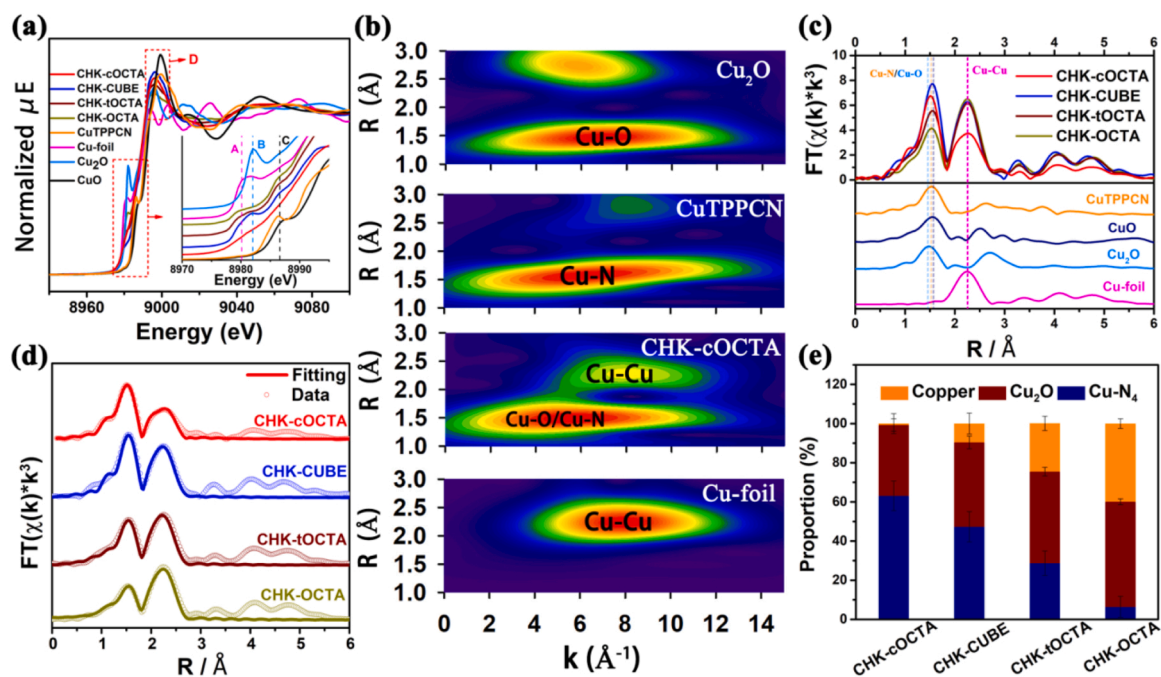


Fig. 3. (a) Normalized Cu K-edge XANES spectra of Cu-based nanoreactors and CuO, Cu<sub>2</sub>O, CuTPPCN, Cu-foil standard, (b) Cu K-edge wavelet transform EXAFS 2D plots of CHK-cOCTA and Cu<sub>2</sub>O, CuTPPCN, Cu-foil standard, (c) Cu K-edge Fourier transform (FT) EXAFS spectra of Cu-based nanoreactors and Cu<sub>2</sub>O, CuTPPCN, CuO, Cu-foil standard, (d) the fitting curves of Fourier transformation of EXAFS spectra for Cu-based nanoreactors, (e) the content proportion of Cu, Cu<sub>2</sub>O and Cu-N<sub>4</sub> in different Cu-based nanoreactors (calculated by LCF of XANES data).

to the formation of larger Cu NPs. The binding energies of Cu (0) and Cu (I) were very close and it was difficult to distinguish Cu (0) and Cu (I) from Cu 2p spectra. Therefore, Auger electron spectroscopy (AES) of the Cu LMM signal was also conducted to provide greater discrimination between the Cu oxidation states. As shown in Fig. 2c, the signal of Cu (0) only exhibited a tailing peak, which was common for Cu NPs in multi-component Cu-based catalysts [36]. Conversely, Cu (I) exhibited a stronger peak indicating that the peak of Cu (0 or I) in Cu 2p spectra was mainly associated with Cu (I). Also of note, the Cu (II) peak in AES was located at 570.7 eV different from CuO (569.6 eV), showing the possible existence of Cu-N<sub>x</sub> in the framework [37]. Additionally, a Cu-N-C characteristic peak was presented at 399.6 eV in the N 1s spectra (Fig. S5), which proved that the Cu (II) was coordinated with the doped-N in carbon framework [32].

X-ray absorption near edge structure (XANES) and X-ray absorption fine structure (EXAFS) spectra were also carried out to further probe the chemical composition and electronic structure of Cu-based nanoreactors. The Cu L<sub>3</sub>-edge adsorption edges of CHK-cOCTA exhibited both Cu (II) and Cu (I) signals at 932.1 and 935.2 eV, respectively (Fig. 2d). The signal of Cu (0) could not be found due to the low intensity of characteristic peak of Cu (0) under the mixed valence state [38]. With the formation of larger Cu (0) nanoparticle, the CHK-CUBE sample exhibited a weak Cu (0) signal in Cu L<sub>3</sub>-edge adsorption edges (Fig. S6). However, the XPS spectra and Cu L<sub>3</sub>-edge adsorption spectra just characterised the surface information of Cu-based nanoreactors. Therefore, the Cu K-edge XANES spectra was further taken to probe the bulk-averaged view of nanoreactors. For the Cu-based materials, the signals between 8970 and 9000 eV provided important information about valence states and electronic structure (Fig. 3a). Taking Cu-foil, Cu<sub>2</sub>O, CuO and CuTPPCN (Cu-N<sub>4</sub> standard structure, shown in Fig. S7) standards as reference, they exhibited the rising-edge shoulders (denoted as A, B and C) and a well-defined white line (WL) peak (denoted as D), respectively. The A shoulder located at nearly 8980 eV was considered the 1s to 4p transition for Cu (0) and the B and C shoulders at 8982 and 8987 eV were characteristics of Cu (I) and Cu (II) [39]. The obtained nanoreactors all exhibited the signals of Cu (0), Cu (I) and Cu (II) (A, B, C shoulders). Meanwhile, the position of the first shoulder peak gradually biased from B to A from CHK-cOCTA to CHK-OCTA, indicating the increase of Cu (0) content. The WL peak intensity was influenced by the coordination structure of metal central atom and the Cu and Cu<sub>2</sub>O NPs had little contribution to the enhancement of the WL peaks [40]. Therefore, the higher WL peak in CHK-cOCTA and CHK-CUBE was attributed to the coordinated Cu (II).

In order to further confirm the existence of Cu-N<sub>x</sub>, the Cu K-edge wavelet transform (WT) EXAFS with powerful resolution in both k and R spaces was applied. As shown in Fig. 3b and Fig. S8, all the Cu-based nanoreactors presented two main lobes. The first one was located in (0–10) Å<sup>-1</sup> and (1.1–1.7) Å area and the second one was in (5–11) Å<sup>-1</sup> and (2–2.5) Å range. The location of second lobe was consistent with the Cu-foil, which could be defined as the Cu-Cu coordination contributed by Cu NPs. This lobe showed an obvious increase from CHK-cOCTA to CHK-OCTA (Fig. 3b and Fig. S8) with the increasing content of Cu NPs in the framework. Due to the broadening effect, it was hard to discriminate the Cu-O/Cu-N contribution clearly by comparing the k-values location in low-R area. However, the first lobe of CHK-cOCTA shifted slightly to lower R-space than Cu<sub>2</sub>O standard, which was much more close to the CuTPPCN model compound. The Fourier transform (FT) EXAFS spectra of Cu-based nanoreactors and Cu-foil, CuO, CuTPPCN, Cu<sub>2</sub>O standard were illustrated in Fig. 3c. All the samples showed a characteristic peak of Cu-Cu scattering consistent with the Cu-foil (at ca. 2.2 Å). According to the Cu<sub>2</sub>O and CuTPPCN standard, the first peak of the nanoreactors at 1.5 Å might be attributed to both Cu-O and Cu-N coordination. For further discerning O and N contributions [41,42], the Debye-Waller (DW) factor of Cu-N path was confirmed by the fitting result (Fig. S9 and Table S1) of CuTPPCN and fixed at 0.003 in the following EXAFS fitting process. The R space (Fig. 3d) and k space (Fig. S10) fitting curves

of Cu-based nanoreactors matched quite well with the experiment spectra and the fitting results of coordination were collected in Table S1. All the nanoreactors exhibited Cu-N, Cu-O and Cu-Cu coordination, which were ascribed to Cu-N<sub>4</sub> single-atom sites, Cu<sub>2</sub>O NPs and Cu NPs, respectively. The lower coordination number of Cu-N, Cu-O and Cu-Cu paths was caused by different content of Cu-based components. Therefore, the linear combination fitting (LCF) of XANES data was applied to quantitative analysis the content of each Cu-based components. The CuTPPCN, Cu<sub>2</sub>O and Cu-foil were taken as standard samples, and the fitting results were displayed in Fig. S11. As shown in Fig. 3e, the content of Cu/Cu<sub>2</sub>O/Cu-N<sub>4</sub> component varied greatly from CHK-cOCTA to CHK-OCTA. The CHK-cOCTA contained a highest Cu-N<sub>4</sub> content of 63%, while the CHK-OCTA got a highest Cu content of 40%, which was consistent with the results of PXRD and XPS spectra. The morphology of MOFs precursor played an important role on the actual chemical composition of Cu-based nanoreactors.

The specific surface area and pore structure of the Cu-based nanoreactors were measured from N<sub>2</sub> adsorption-desorption isotherm based on Brunauer-Emmett-Teller (BET) method. As shown in Fig. 4a, all the nanoreactors exhibited the IV-typed isotherm with H3-typed hysteresis loop, indicating the existence of mesopores. The CHK-cOCTA exhibited highest specific surface areas and pore volume (Fig. 4b, Table S2) without the occupation of pores by Cu NPs. Such difference in pore structures influenced the chemisorbed capacity and the CHK-cOCTA displayed a highest CO<sub>2</sub> adsorption capacity about 19.3 cm<sup>3</sup>/g (Fig. 4c). The CO<sub>2</sub> temperature-programmed desorption (CO<sub>2</sub>-TPD) measurement was further applied to assess the CO<sub>2</sub> activation capacity of Cu-based nanoreactors. All these nanoreactors showed a major peak in moderate acid strength area (Fig. 4d). The peak at 350 °C was ascribed to the HCO<sub>2</sub> desorption, indicating the adsorption of \*COOH on the catalyst surface, which was the most classic model of CO<sub>2</sub> molecule adsorption in electrocatalytic CO<sub>2</sub>RR process [43,44]. The HCO<sub>2</sub> desorption peak of CHK-cOCTA shifted slightly to higher temperature, indicating a better CO<sub>2</sub> activation ability. In addition, the peak area of CHK-cOCTA was a little larger than others. It proved a better CO<sub>2</sub> adsorption capacity of CHK-cOCTA, which was coincident with CO<sub>2</sub> adsorption result. As is well known, the mass transfer and activate capacity were crucial for catalyst [45,46]. The high specific surface area and the porous structure were beneficial for exposing more active sites and facilitating the transfer of the reactant/product.

### 3.2. Catalytic performance of Cu-based nanoreactors for CO<sub>2</sub>RR

The electrochemical performance of Cu-based nanoreactors was evaluated by linear sweep voltammetry (LSV) scanning in a CO<sub>2</sub>-saturated 0.1 M KHCO<sub>3</sub>/0.1 M KCl electrolyte. As shown in Fig. 5a, all the Cu-based nanoreactors exhibited a Cu (II) to Cu (I) reduction peak at ca. -0.9 V vs. reversible hydrogen electrode (RHE) [47]. The CO<sub>2</sub>RR catalytic activity of CHK-cOCTA outperformed other samples since a higher current density was generated in the potential ranged from -1.0 V to -1.6 V. When the LSV curve was tested in Ar-saturated electrolyte, the current density reduced sharply, indicating that the catalysts were more favorable for CO<sub>2</sub>RR than hydrogen evolution reaction (HER, inset of Fig. 5a). Electrochemical impedance spectroscopy (EIS) was conducted to investigate electron transfer processes (Fig. 5b). According to the fitting result (Table S3), the CHK-cOCTA exhibited the lowest charge transfer resistance (*R<sub>ct</sub>*) of 2.4 Ω, which manifested CHK-cOCTA had less polarization loss and higher electronic interaction at the reaction interfaces during CO<sub>2</sub> electroreduction. It was believed that the higher specific surface area and the optimized porous structure of CHK-cOCTA promoted mass transfer and exposed more active sites, which was both benefit for CO<sub>2</sub> activation and thus resulted in high catalytic performance in CO<sub>2</sub>RR.

To evaluate the electrocatalytic selectivity, the gas chromatography (GC) was used to determine the components of the gas products and the nuclear magnetic (NMR) on the electrolyte after the reaction was used to

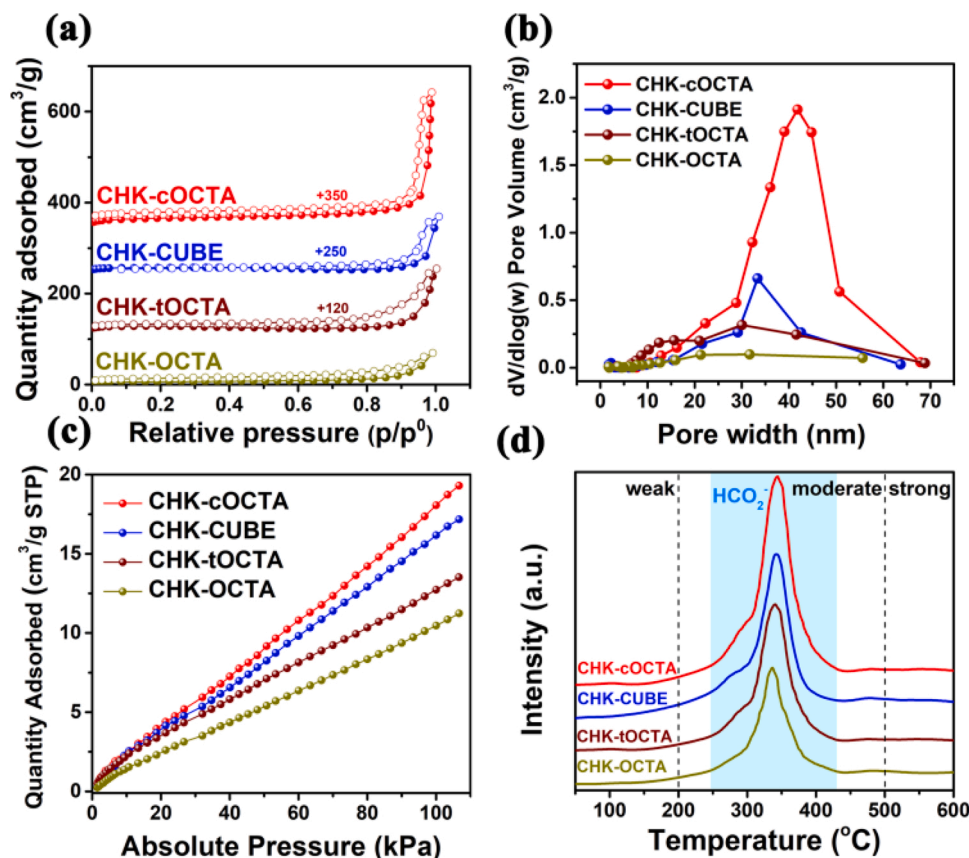


Fig. 4. (a) N<sub>2</sub> adsorption-desorption, (b) BJH pore distributions, (c) CO<sub>2</sub> adsorption isotherms, and (d) CO<sub>2</sub>-TPD results of Cu-based nanoreactors.

analyze the liquid products. All samples produced gas products such as H<sub>2</sub>, CO, CH<sub>4</sub>, C<sub>2</sub>H<sub>4</sub> and no liquid product could be found in <sup>1</sup>H NMR (Fig. S12a-d). As shown in Fig. 5c, the CHK-cOCTA exhibited better catalytic activity and selectivity toward CO<sub>2</sub>RR. The Faradic efficiency (FE) of gas products at different potentials was shown in Fig. 5d and Fig. S13. Increasing the proportion of Cu NPs, the competition of HER improved significantly. Meanwhile, the FE selectivity of CO also impaired obviously when the content of Cu-N<sub>4</sub> single-atom sites decreased. Among all Cu-based nanoreactors, the selectivity of CHK-cOCTA for deep reduction products (CH<sub>4</sub> and C<sub>2</sub>H<sub>4</sub>) reached up to ca. 80% (at -1.5 V vs. RHE), and the selectivity for CH<sub>4</sub> was nearly 60% (at -1.6 V vs. RHE), which was a high-level efficiency in previous reported work (Table S4). The partial current density of CH<sub>4</sub> ( $J_{CH_4}$ ) reached to 25 mA cm<sup>-2</sup> in the H-typed cell test, which was obviously higher than that of the previously reported catalyst (Table S4). The long-term stability of CHK-cOCTA was maintained for a continuous reduction 20 h at -1.5 V vs. RHE. The FE selectivity for liquid product was less than 1% during the durability test (Fig. S12e). The CHK-cOCTA showed a good stability and remained 64% FE selectivity toward CO<sub>2</sub>RR. In consideration of the negative potential will accelerate the reduction of Cu species, the XPS spectra, PXRD spectra and TEM images were applied to verified the change of active sites in durability test. Compared with the original spectra of CHK-cOCTA (Fig. 2b), the characteristic of Cu-N<sub>4</sub> did not show obvious change in both Cu 2p and N 1s spectra, which indicated that the Cu-N<sub>4</sub> single-atom structure was stabilized during long-term durability test (Fig. S14). However, as shown in PXRD spectra in Fig. S15, the intensity of Cu<sub>2</sub>O phase decreased while the intensity of Cu phase increased with the durability test processing. Moreover, the TEM images of CHK-cOCTA after 5, 10 and 20 h durability test (Fig. S16) also showed the gradually formation of larger Cu NPs. Combining with the change of current density and FE, the decrease of catalytic performance was due to the disappearance of Cu<sub>2</sub>O active sites and the agglomeration

of larger Cu NPs.

### 3.3. Tandem catalytic mechanism of CHK-cOCTA for CO<sub>2</sub>RR

To clarify the catalytic mechanism of CHK-cOCTA, the contrast sample CHK-1 was pyrolyzed from the raw HKUST-1 precursor without triethylamine modification. Surveyed by the PXRD pattern (Fig. S17) and XPS spectra (Fig. S18), CHK-1 only displayed the characteristic of Cu NPs. Comparing their catalytic performance, it was noticeable that CHK-1 exhibited a poor performance due to the lack of Cu-N<sub>4</sub> and Cu<sub>2</sub>O active sites (Fig. S19 and Figure 20). In particular, the CO faradic efficiency of CHK-1 was obviously lower than CHK-cOCTA at low overpotential (Figure S17 and Fig. 5d). The CO<sub>2</sub> activation capacity and CO<sub>2</sub>RR catalytic performance both displayed a significant increase when the Cu-N<sub>4</sub> sites were introduced. It was credible to deduce that the Cu-N<sub>4</sub> active sites might produce CO from CO<sub>2</sub>. In addition, the sole Cu<sub>2</sub>O active sites were rarely reported to exhibit exclusive catalytic selectivity toward CH<sub>4</sub> in the previous work [48]. However, Cu<sub>2</sub>O active sites in CHK-cOCTA were obviously beneficial to the CH<sub>4</sub> product in our work. In order to ascertain the mechanistic insight for such difference, the *in-situ* attenuated total reflection Fourier transform infrared spectra (ATR-FTIR) and density theoretical theory (DFT) calculation were further performed.

The *in-situ* ATR-FTIR measurement was proceeded in the home-made cell (Fig. S21) under a lower overpotential (-1.1 V vs. RHE) firstly to ascertain the intermediates during CO<sub>2</sub>RR. As shown in Fig. S22, the band located at 1641 cm<sup>-1</sup>, 1533 cm<sup>-1</sup>, 1410 cm<sup>-1</sup> and 1341 cm<sup>-1</sup> were assigned to the \*OH<sub>2</sub>, \*OC<sub>2</sub>O, \*COOH (symm) and \*COOH (C-O) respectively corresponding to the adsorption of H<sub>2</sub>O, carbonate ion and CO<sub>2</sub> [49–51]. The chemisorbed CO (\*CO) peak on CHK-cOCTA was appeared at 1740 cm<sup>-1</sup> [52] and the signal of \*CO gradually enhanced in the reaction progress, which indicated the accumulation of \*CO



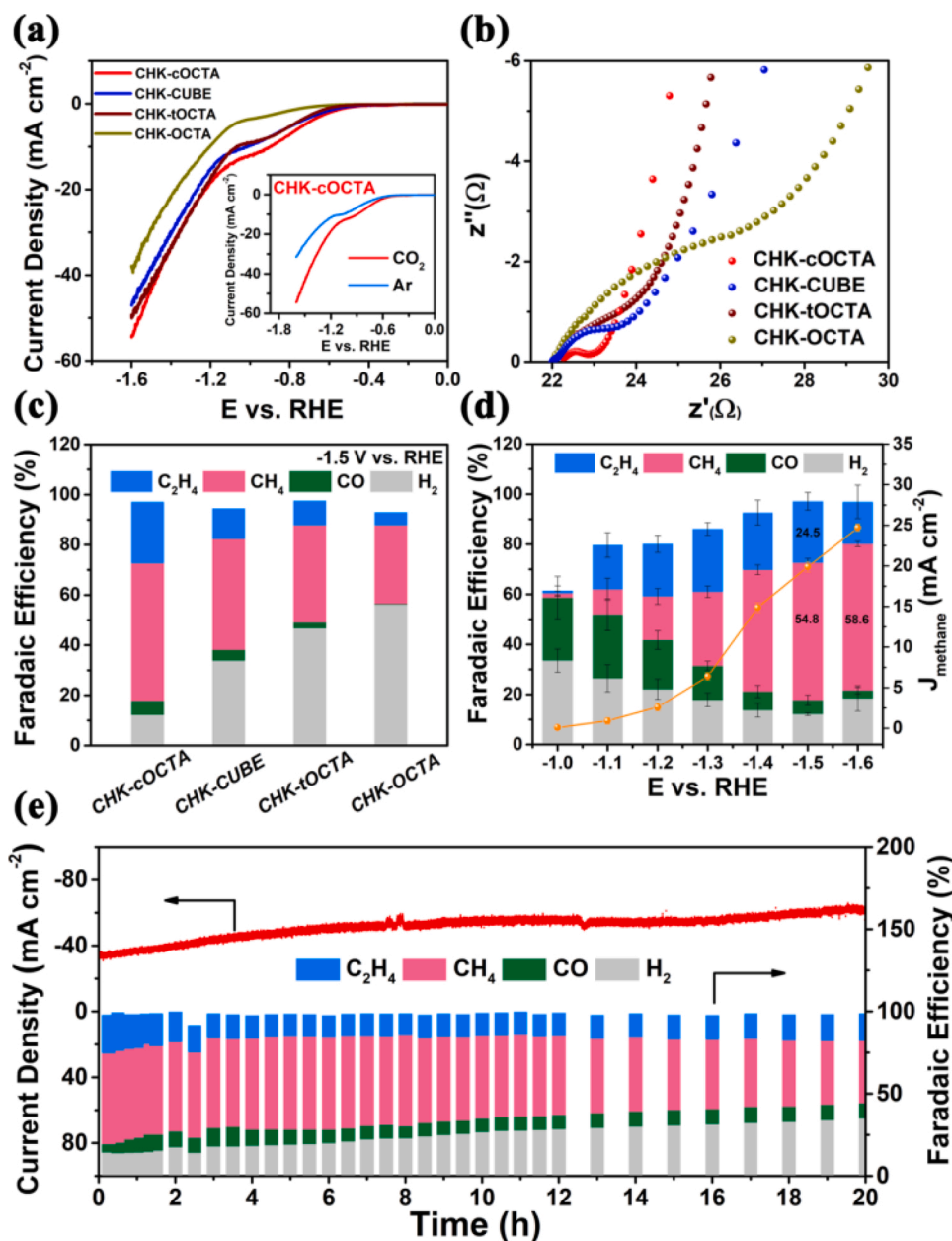


**Fig. 5.** (a) LSV curves of Cu-based nanoreactors in  $\text{CO}_2$ -saturated  $0.1\text{ M KHCO}_3/0.1\text{ M KCl}$  mixture solution (inset: LSV curves of CHK-cOCTA in Ar-saturated  $0.1\text{ M KHCO}_3/0.1\text{ M KCl}$  mixture solution), (b) Electrochemical impedance spectra (EIS) of Cu-based nanoreactors, (c) Faradaic efficiency of Cu-based nanoreactors at  $-1.5\text{ V vs. RHE}$ , (d) Faradaic efficiency and  $\text{CH}_4$  partial current density of CHK-cOCTA at different potentials, (e) Catalytic durability of CHK-cOCTA at  $-1.5\text{ V vs. RHE}$  for 20 h.

intermediate. There also presented the signal of  $^*\text{COH}$  ( $1054\text{ cm}^{-1}$ ), which was the intermediate of the reduction of  $\text{CO}_2$  to  $\text{C}_2\text{H}_4$  [11]. Combined with the FE selectivity of CHK-cOCTA at  $-1.1\text{ V vs. RHE}$  (Fig. 5d) above, the observations of ATR-FTIR indicated that the high CO selectivity at low overpotential might attribute to the accumulation of the  $^*\text{CO}$  intermediate in the active sites. In addition, the ATR-FTIR measurement was also proceeded under a higher overpotential ( $-1.5\text{ V vs. RHE}$ ). As shown in Fig. 6a, the bands located at  $1471\text{ cm}^{-1}$ ,  $1392\text{ cm}^{-1}$  and  $1210\text{ cm}^{-1}$  could be assigned to  $^*\text{CH}_2\text{O}$ ,  $^*\text{OCH}_3$  and  $^*\text{CHO}$  respectively, which were the crucial intermediates from  $\text{CO}_2$  to  $\text{CH}_4$  in  $\text{CO}_2\text{RR}$  [47,50,52]. The intensity of  $^*\text{COH}$  signal decreased obviously indicating the suppression of  $\text{CO}_2$  to  $\text{C}_2\text{H}_4$  under  $-1.5\text{ V vs. RHE}$ . It was worth noting that no visible  $^*\text{CO}$  signal could be found under this potential during the reaction progress. Considering the existence of CO product at this potential (Fig. 5d), the absence of  $^*\text{CO}$  signal might be due to the fast desorption from Cu- $\text{N}_4$  sites and re-adsorption on Cu/ $\text{Cu}_2\text{O}$  sites of  $^*\text{CO}$  intermediate during the  $\text{CO}_2$  to  $\text{CH}_4$  catalytic process. The above results suggested that the multicomponent Cu-based

active sites in CHK-cOCTA had synergistically enhanced the formation of  $\text{CH}_4$  via transfer the high concentration of CO generated by Cu- $\text{N}_4$  active sites to the nearby  $\text{Cu}_2\text{O}/\text{Cu}$  NP active sites, which might work in a tandem way [24].

In order to reveal the tandem catalytic mechanism of CHK-cOCTA, the DFT calculation was further performed. Based on the experiment results, Cu- $\text{N}_4$  single-atom sites, Cu(111) and  $\text{Cu}_2\text{O}(111)$  were chosen as the model surfaces for DFT calculation. As the core intermediate, the  $^*\text{CO}$  was formed by two electron-proton coupling processes. Here, three competitive pathways could be expanded (Fig. S23-S25). First, CO desorbed to regenerate free active site (Black arrow). Second,  $^*\text{CHO}$  was expected to trigger  $\text{CH}_4$  formation through hydrogenation of  $^*\text{CO}$  (Blue arrow). Third,  $^*\text{OCCO}$  was generated by CO dimerization, leading to  $\text{C}_2\text{H}_4$  formation (Red arrow). The rate-determined steps (RDS) of these three pathways were CO desorbed,  $^*\text{CHO}$  formed from  $^*\text{CO}$  and  $^*\text{OCCO}$  generated through  $^*\text{CO}$  coupling, respectively. Comparing the step of  $^*\text{CO}$  desorption (Fig. 6b), Cu- $\text{N}_4$  sites displayed a lowest desorption energy ( $0.03\text{ eV}$ ), therefore the produced CO could be quickly released

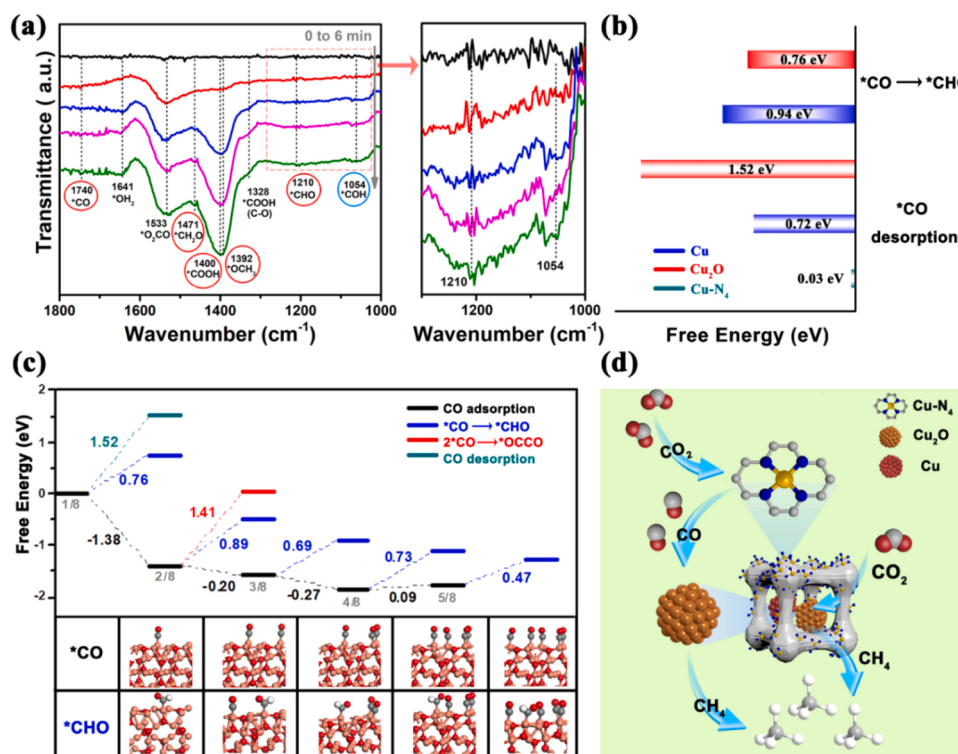


**Fig. 6.** (a) *in-situ* ATR-FTIR spectra of CHK-cOCTA tested at  $-1.5$  V vs. RHE in CO<sub>2</sub>-saturated 0.1 M KHCO<sub>3</sub>/ 0.1 M KCl mixture solution; (b) the free energy of \*CO to \*CHO and \*CO desorption on Cu-N<sub>4</sub>, Cu(111) and Cu<sub>2</sub>O(111), respectively; (c) the free energy of RDS with different \*CO coverage on Cu<sub>2</sub>O(111); (d) schematic illustration of the CO<sub>2</sub> to CH<sub>4</sub> reaction pathway in CHK-cOCTA nanoreactor.

from Cu-N<sub>4</sub> sites and then transfer to Cu<sub>2</sub>O(111) and Cu(111) sites for further reduction. Furthermore, the free energy of \*CHO formation (0.76 eV) was much lower than the CO desorption (1.52 eV) in Cu<sub>2</sub>O (111) surface, which supposed that the CO produced from Cu-N<sub>4</sub> could be effectively transferred to Cu<sub>2</sub>O(111) surface for deep hydrogenation. The DFT calculation result was consistent with the experiment result, suggesting that the Cu-N<sub>4</sub> active sites and Cu<sub>2</sub>O/Cu NPs worked in a tandem way to control the electrochemical reduction of CO<sub>2</sub> to CH<sub>4</sub>.

In addition, the previous result proved that 36% Cu-based site was Cu<sub>2</sub>O in CHK-cOCTA, meanwhile the content of Cu was only 1%. Therefore the attention was focus on the reaction process on Cu<sub>2</sub>O(111) surface. Compared the free energy of the RDS intermediates (Fig. 6c), the production of CH<sub>4</sub> was favored than C<sub>2</sub>H<sub>4</sub> on Cu<sub>2</sub>O(111) surface. Therefore, the influence of the \*CO coverage on Cu<sub>2</sub>O(111) surface for CH<sub>4</sub> product was studied intensively. When the \*CO coverage rose from 2/8 (two CO molecules to eight Cu atoms of catalysis surface) to 5/8 on Cu<sub>2</sub>O(111) surface, the free energy of \*CO hydrogenated into \*CHO decreased from 0.89 eV to 0.47 eV. The higher concentration of \*CO created by Cu-N<sub>4</sub> sites could induce the formation of CH<sub>4</sub> on Cu<sub>2</sub>O(111) surface efficiently. In general, the DFT calculations and the operando ATR-FTIR results were consistent with our proposed tandem catalysis mechanism that the CO molecules produced from Cu-N<sub>4</sub> active sites migrated to the nearby Cu<sub>2</sub>O(111) surface to form a high coverage of \*CO, which induced the reduction of CH<sub>4</sub> on Cu<sub>2</sub>O(111) surface (Fig. 6d).

#### 4. Conclusions

In summary, the chemical composition of the Cu-based nanoreactors can be regulated effectively by adjusting the geometrical morphology of MOFs precursors. The optimized pore structure and high content of Cu-N<sub>4</sub>/Cu<sub>2</sub>O active sites make CHK-cOCTA exhibit excellent catalytic performance in CO<sub>2</sub>RR. Moreover, the tandem catalytic mechanism of multicomponent active sites was elucidated intensively based on the chemical composition characterization, *in-situ* ATR-FTIR spectra and

DFT calculation. The CO<sub>2</sub> molecules were reduced to CO molecules firstly catalyzed by Cu-N<sub>4</sub> sites. Then the CO molecules were transferred to Cu<sub>2</sub>O/Cu sites for further deep reduction. The higher concentration of \*CO created by Cu-N<sub>4</sub> sites could decrease the free energy of RDS and induced the formation of CH<sub>4</sub> on Cu<sub>2</sub>O(111) surface efficiently. This work provides a promising direction for designing and synthesizing multicomponent Cu-based tandem catalysts to access high efficiency and selectivity in the electrocatalytic CO<sub>2</sub> reduction reaction.

#### Appendix A. Supplementary data

Density Functional Theory (DFT) calculation methods; SEM images; PXRD patterns; TG curve images; EDS spectra; XPS Cu 2p and N 1s spectra; Cu L-edge XANES spectrum; Chemical structure of Cu-TPPCN; Cu K-edge WT-EXAFS 2D plots; Cu K-edge EXAFS and curvefit in  $k^3$ -weighted  $k$ -space and  $R$ -space; Linear combination fitting (LCF) of the XANES data; <sup>1</sup>H NMR spectra of the electrolyte; CO<sub>2</sub>RR performance; *in-situ* ATR-FTIR spectra; The CO<sub>2</sub>RR pathway and free energy; Electrochemical impedance spectra (EIS) fitting.

#### CRediT authorship contribution statement

Rong Cao and Hongfang Li supervised the research. Hongfang Li and Wanfang Xiong designed the experiment and wrote the paper. Wanfang Xiong synthesized the materials, performed the catalyst characterizations and catalytic experiments. Duanhui Si conducted the DFT calculation and Yuanbiao Huang provided the supervision for the catalytic mechanism. Jundong Yi performed X-ray absorption near edge structure (XANES) and EXAFS experiments. Rong Cao, Hongfang Li, Yuan-Biao Huang, Wanfang Xiong, Duanhui Si, Jundong Yi contributed to scientific discussion of the article.

## Declaration of Competing Interest

The authors declare that they have no known competing financial interests or personal relationships that could have appeared to influence the work reported in this paper.

## Acknowledgements

We acknowledge the financial support from the National Key Research and Development Program of China (2017YFA0206801 and 2018YFA0704502), NSFC (22171265, 22033008 and 21871263); Fujian Science & Technology Innovation Laboratory for Optoelectronic Information of China (2021ZZ103). We thank beamline BL14W1 of Shanghai Synchrotron Radiation Facilities (SSRF) for providing the beam time.

## Appendix A. Supporting information

Supplementary data associated with this article can be found in the online version at [doi:10.1016/j.apcatb.2022.121498](https://doi.org/10.1016/j.apcatb.2022.121498).

## References

- [1] S. Chu, Y. Cui, N. Liu, The path towards sustainable energy, *Nat. Mater.* 16 (2016) 16–22, <https://doi.org/10.1038/nmat4834>.
- [2] S. Chu, A. Majumdar, Opportunities and challenges for a sustainable energy future, *Nature* 488 (2012) 294–303, <https://doi.org/10.1038/nature11475>.
- [3] D. Gao, F. Cai, G. Wang, X. Bao, Nanostructured heterogeneous catalysts for electrochemical reduction of CO<sub>2</sub>, *Curr. Opin. Green. Sust.* 3 (2017) 39–44, <https://doi.org/10.1016/j.cogsc.2016.10.004>.
- [4] S.B. Varandili, D. Stoian, J. Vavra, K. Rossi, J.R. Pankhurst, Y.T. Guntern, N. Lopez, R. Buonsanti, Elucidating the structure-dependent selectivity of Cu/Zn towards methane and ethanol in CO<sub>2</sub> electroreduction using tailored Cu/ZnO precatalysts, *Chem. Sci.* 12 (2021) 14484–14493, <https://doi.org/10.1039/d1sc04271h>.
- [5] S. Zhao, Y. Wang, J. Dong, C.-T. He, H. Yin, P. An, K. Zhao, X. Zhang, C. Gao, L. Zhang, J. Lv, J. Wang, J. Zhang, A.M. Khattak, N.A. Khan, Z. Wei, J. Zhang, S. Liu, H. Zhao, Z. Tang, Ultrathin metal-organic framework nanosheets for electrocatalytic oxygen evolution, *Nat. Energy* 1 (2016) 1–10.
- [6] H. Ou, D. Wang, Y. Li, How to select effective electrocatalysts: nano or single atom? *Nano Sel.* 2 (2020) 492–511, <https://doi.org/10.1002/nano.202000239>.
- [7] O.S. Bushuyev, P. De Luna, C.T. Dinh, L. Tao, G. Saur, J. van de Lagemaat, S. O. Kelley, E.H. Sargent, What should we make with CO<sub>2</sub> and how can we make it? *Joule* 2 (2018) 825–832, <https://doi.org/10.1016/j.joule.2017.09.003>.
- [8] X. Sun, Y. Tuo, C. Ye, C. Chen, Q. Lu, G. Li, P. Jiang, S. Chen, P. Zhu, M. Ma, J. Zhang, J.H. Bitter, D. Wang, Y. Li, Phosphorus induced electron localization of single iron sites for boosted CO<sub>2</sub> electroreduction reaction, *Angew. Chem. Int. Ed.* 60 (2021) 23614–23618, <https://doi.org/10.1002/anie.202110433>.
- [9] P. De Luna, C. Hahn, D. Higgins, S.A. Jaffer, T.F. Jaramillo, E.H. Sargent, What would it take for renewably powered electrolysis to displace petrochemical processes? *Science* 364 (2019) eaav3506, <https://doi.org/10.1126/science.aav3506>.
- [10] Q. Wu, R.-K. Xie, M.-J. Mao, G.-L. Chai, J.-D. Yi, S.-S. Zhao, Y.-B. Huang, R. Cao, Integration of strong electron transporter tetrathiafulvalene into metalloporphyrin-based covalent organic framework for highly efficient electroreduction of CO<sub>2</sub>, *ACS Energy Lett.* 5 (2020) 1005–1012, <https://doi.org/10.1021/acsenenerglett.9b02756>.
- [11] A. Vasileff, C. Xu, Y. Jiao, Y. Zheng, S.-Z. Qiao, Surface and interface engineering in copper-based bimetallic materials for selective CO<sub>2</sub> electroreduction, *Chem* 4 (2018) 1809–1831, <https://doi.org/10.1016/j.chempr.2018.05.001>.
- [12] S. Nitopi, E. Bertheussen, S.B. Scott, X. Liu, A.K. Engstfeld, S. Horch, B. Seger, I.E. L. Stephens, K. Chan, C. Hahn, J.K. Nørskov, T.F. Jaramillo, I. Chorkendorff, Progress and perspectives of electrochemical CO<sub>2</sub> reduction on copper in aqueous electrolyte, *Chem. Rev.* 119 (2019) 7610–7672, <https://doi.org/10.1021/acs.chemrev.8b00705>.
- [13] X. Chen, D.A. Henckel, U.O. Nwabara, Y. Li, A.I. Frenkel, T.T. Fister, P.J.A. Kenis, A.A. Gewirth, Controlling speciation during CO<sub>2</sub> reduction on Cu-Alloy electrodes, *ACS Catal.* 10 (2019) 672–682, <https://doi.org/10.1021/acscatal.9b04368>.
- [14] M. Li, Y. Ma, J. Chen, R. Lawrence, W. Luo, M. Sacchi, W. Jiang, J. Yang, Residual chlorine induced cationic active species on a porous copper electrocatalyst for highly stable electrochemical CO<sub>2</sub> reduction to C<sub>2+</sub>, *Angew. Chem. Int. Ed.* 60 (2021) 11487–11493, <https://doi.org/10.1002/anie.202102606>.
- [15] Z. Yin, C. Yu, Z. Zhao, X. Guo, M. Shen, N. Li, M. Muzzio, J. Li, H. Liu, H. Lin, J. Yin, G. Lu, D. Su, S. Sun, Cu<sub>3</sub>N nanocubes for selective electrochemical reduction of CO<sub>2</sub> to ethylene, *Nano Lett.* 19 (2019) 8658–8663, <https://doi.org/10.1021/acs.nanolett.9b03324>.
- [16] X. Chang, T. Wang, Z.J. Zhao, P. Yang, J. Greeley, R. Mu, G. Zhang, Z. Gong, Z. Luo, J. Chen, Y. Cui, G.A. Ozin, J. Gong, Tuning Cu/Cu<sub>2</sub>O interfaces for the reduction of carbon dioxide to methanol in aqueous solutions, *Angew. Chem. Int. Ed.* 57 (2018) 15415–15419, <https://doi.org/10.1002/anie.201805256>.
- [17] N.-T. Suen, Z.-R. Kong, C.-S. Hsu, H.-C. Chen, C.-W. Tung, Y.-R. Lu, C.-L. Dong, C.-C. Shen, J.-C. Chung, H.M. Chen, Morphology manipulation of copper nanocrystals and product selectivity in the electrocatalytic reduction of carbon dioxide, *ACS Catal.* 9 (2019) 5217–5222, <https://doi.org/10.1021/acscatal.9b00790>.
- [18] T. Moller, F. Scholten, T.N. Thanh, I. Sinev, J. Timoshenko, X. Wang, Z. Jovanov, M. Gliech, B. Roldan Cuenya, A.S. Varela, P. Strasser, Electrocatalytic CO<sub>2</sub> reduction on CuO<sub>x</sub> nanocubes: tracking the evolution of chemical state, geometric structure, and catalytic selectivity using operando spectroscopy, *Angew. Chem. Int. Ed.* 59 (2020) 17974–17983, <https://doi.org/10.1002/anie.202007136>.
- [19] Y.B. Huang, J. Liang, X.S. Wang, R. Cao, Multifunctional metal-organic framework catalysts: synergistic catalysis and tandem reactions, *Chem. Soc. Rev.* 46 (2017) 126–157, <https://doi.org/10.1039/c6cs00250a>.
- [20] Y. Zhang, L. Jiao, W. Yang, C. Xie, H.L. Jiang, Rational fabrication of low-coordinate single-atom Ni electrocatalysts by MOFs for highly selective CO<sub>2</sub> reduction, *Angew. Chem. Int. Ed.* 60 (2021) 7607–7611, <https://doi.org/10.1002/anie.202016219>.
- [21] R. Chen, W. Yang, M. Cao, H. Li, Synthesis and crystal structure of a new noble metal-containing supramolecular self-assembly with decamethylcucurbit[5]uril, *Chin. J. Struct. Chem.* 39 (2020) 525–542, <https://doi.org/10.14102/j.cnki.0254-5861.2011-2440>.
- [22] M. Zhao, K. Yuan, Y. Wang, G. Li, J. Guo, L. Gu, W. Hu, H. Zhao, Z. Tang, Metal-organic frameworks as selectivity regulators for hydrogenation reactions, *Nature* 539 (2016) 76–80, <https://doi.org/10.1038/nature19763>.
- [23] M. Zhao, K. Deng, L. He, Y. Liu, G. Li, H. Zhao, Z. Tang, Core-shell palladium nanoparticle@metal-organic frameworks for hydrogenation catalysts for cascade reactions, *J. Am. Chem. Soc.* 136 (2014) 1738–1741, <https://doi.org/10.1021/ja411468e>.
- [24] L. Lin, T. Liu, J. Xiao, H. Li, P. Wei, D. Gao, B. Nan, R. Si, G. Wang, X. Bao, Enhancing CO<sub>2</sub> electroreduction to methane with a cobalt phthalocyanine and zinc-nitrogen-carbon tandem catalyst, *Angew. Chem. Int. Ed.* 59 (2020) 22408–22413, <https://doi.org/10.1002/anie.202009191>.
- [25] Y. Wu, N. Xie, X. Li, Z. Fu, X. Wu, Q. Zhu, MOF-derived hierarchical hollow NiRu-C nanohybrid for efficient hydrogen evolution reaction, *Chin. J. Struct. Chem.* 40 (2021) 1346–1356, <https://doi.org/10.14102/j.cnki.0254-5861.2011-3153>.
- [26] F. Zhang, J. Chen, J. Yang, Fiber materials for electrocatalysis applications, *Adv. Fiber Mater.* (2022), <https://doi.org/10.1007/s42765-022-00146-7>.
- [27] Y. Hou, Y.-B. Huang, Y.-L. Liang, G.-L. Chai, J.-D. Yi, T. Zhang, K.-T. Zang, J. Luo, R. Xu, H. Lin, S.-Y. Zhang, H.-M. Wang, R. Cao, Unraveling the reactivity and selectivity of atomically isolated metal-nitrogen sites anchored on porphyrinic triazine frameworks for electroreduction of CO<sub>2</sub>, *CCS Chem.* 1 (2019) 384–395, <https://doi.org/10.31635/ccschem.019.20190011>.
- [28] W. Xiong, H. Li, H. Wang, J. Yi, H. You, S. Zhang, Y. Hou, M. Cao, T. Zhang, R. Cao, Hollow mesoporous carbon sphere loaded Ni-N<sub>4</sub> single-atom: support structure study for CO<sub>2</sub> electrocatalytic reduction catalyst, *Small* 16 (2020), e2003943, <https://doi.org/10.1002/sml.202003943>.
- [29] H. Tian, J. Liang, J. Liu, Nanoengineering carbon spheres as nanoreactors for sustainable energy applications, *Adv. Mater.* 31 (2019), e1903886, <https://doi.org/10.1002/adma.201903886>.
- [30] P. Yin, T. Yao, Y. Wu, L. Zheng, Y. Lin, W. Liu, H. Ju, J. Zhu, X. Hong, Z. Deng, G. Zhou, S. Wei, Y. Li, Single cobalt atoms with precise N-coordination as superior oxygen reduction reaction catalysts, *Angew. Chem. Int. Ed.* 55 (2016) 10800–10805, <https://doi.org/10.1002/anie.201604802>.
- [31] D. Tan, J. Zhang, L. Yao, X. Tan, X. Cheng, Q. Wan, B. Han, L. Zheng, J. Zhang, Multi-shelled CuO microboxes for carbon dioxide reduction to ethylene, *Nano Res.* 13 (2020) 768–774, <https://doi.org/10.1007/s12274-020-2692-1>.
- [32] H. Shang, X. Zhou, J. Dong, A. Li, X. Zhao, Q. Liu, Y. Lin, J. Pei, Z. Li, Z. Jiang, D. Zhou, L. Zheng, Y. Wang, J. Zhou, Z. Yang, R. Cao, R. Sarangi, T. Sun, X. Yang, X. Zheng, W. Yan, Z. Zhuang, J. Li, W. Chen, D. Wang, J. Zhang, Y. Li, Engineering unsymmetrically coordinated Cu-S<sub>3</sub>N<sub>3</sub> single atom sites with enhanced oxygen reduction activity, *Nat. Commun.* 11 (2020) 3049, <https://doi.org/10.1038/s41467-020-16848-8>.
- [33] Q. Liu, J.-M. Yang, L.-N. Jin, W.-Y. Sun, Metal ion induced porous HKUST-1 nano/microcrystals with controllable morphology and size, *CrystEngComm* 18 (2016) 4127–4132, <https://doi.org/10.1039/c5ce02497h>.
- [34] J. Zhang, H. Lin, Q. Kuang, Z. Xie, Toward rationally designing surface structures of micro- and nanocrystallites: role of supersaturation, *Acc. Chem. Res.* 51 (2018) 2880–2887, <https://doi.org/10.1021/acs.accounts.8b00344>.
- [35] H.X. Lin, Z.C. Lei, Z.Y. Jiang, C.P. Hou, D.Y. Liu, M.M. Xu, Z.Q. Tian, Z.X. Xie, Supersaturation-dependent surface structure evolution: from ionic, molecular to metallic micro/nanocrystals, *J. Am. Chem. Soc.* 135 (2013) 9311–9314, <https://doi.org/10.1021/ja404371k>.
- [36] S.Y. Lee, H. Jung, N.K. Kim, H.S. Oh, B.K. Min, Y.J. Hwang, Mixed copper states in anodized Cu electrocatalyst for stable and selective ethylene production from CO<sub>2</sub> reduction, *J. Am. Chem. Soc.* 140 (2018) 8681–8689, <https://doi.org/10.1021/jacs.8b02173>.
- [37] P.M.P.S. Poulston, P. Stone, M. Bowker\*, Surface oxidation and reduction of CuO and Cu<sub>2</sub>O studied using XPS and XAES, *Surf. Interface Anal.* 24 (1996) 811–820, [https://doi.org/10.1002/\(SICI\)1096-9918\(199611\)24:12<811::AID-SIA191>3.0.CO;2-Z](https://doi.org/10.1002/(SICI)1096-9918(199611)24:12<811::AID-SIA191>3.0.CO;2-Z).
- [38] T.C. Chou, C.C. Chang, H.L. Yu, W.Y. Yu, C.L. Dong, J.J. Velasco-Velez, C. H. Chuang, L.C. Chen, J.F. Lee, J.M. Chen, H.L. Yu, Controlling the oxidation state of the Cu electrode and reaction intermediates for electrochemical CO<sub>2</sub> reduction to ethylene, *J. Am. Chem. Soc.* 142 (2020) 2857–2867, <https://doi.org/10.1021/jacs.9b11126>.



- [39] K.-i. Shimizu, H. Maeshima, H. Yoshida, A. Satsuma, T. Hattori, Ligand field effect on the chemical shift in XANES spectra of Cu(II) compounds, *Phys. Chem. Chem. Phys.* 3 (2001) 862–866, <https://doi.org/10.1039/b007276l>.
- [40] A. Gaur, B.D. Shrivastava, S.K. Joshi, Copper K-edge XANES of Cu(I) and Cu(II) oxide mixtures, *J. Phys. Conf. Ser.* 190 (2009), 012084, <https://doi.org/10.1088/1742-6596/190/1/012084>.
- [41] I.A. Pankin, A. Martini, K.A. Lomachenko, A.V. Soldatov, S. Bordiga, E. Borfecchia, Identifying Cu-oxo species in Cu-zeolites by XAS: a theoretical survey by DFT-assisted XANES simulation and EXAFS wavelet transform, *Catal. Today* 345 (2020) 125–135, <https://doi.org/10.1016/j.cattod.2019.09.032>.
- [42] C. Negri, T. Selli, E. Borfecchia, A. Martini, K.A. Lomachenko, T.V.W. Janssens, M. Cutini, S. Bordiga, G. Berlier, Structure and reactivity of oxygen-bridged diamino dicopper(II) complexes in Cu-ion-exchanged chabazite catalyst for  $\text{NH}_3$ -mediated selective catalytic reduction, *J. Am. Chem. Soc.* 142 (2020) 15884–15896, <https://doi.org/10.1021/jacs.0c06270>.
- [43] Y. Pu, Y. Luo, X. Wei, J. Sun, L. Li, W. Zou, L. Dong, Synergistic effects of  $\text{Cu}_2\text{O}$ -decorated  $\text{CeO}_2$  on photocatalytic  $\text{CO}_2$  reduction: Surface Lewis acid/base and oxygen defect, *Appl. Catal. B: Environ.* 254 (2019) 580–586, <https://doi.org/10.1016/j.apcatb.2019.04.093>.
- [44] S. Zhu, T. Li, W.-B. Cai, M. Shao,  $\text{CO}_2$  electrochemical reduction as probed through infrared spectroscopy, *ACS Energy Lett.* 4 (2019) 682–689, <https://doi.org/10.1021/acseenergylett.8b02525>.
- [45] W. Xiong, H. Li, H. You, M. Cao, R. Cao, Encapsulating metal organic framework into hollow mesoporous carbon sphere as efficient oxygen bifunctional electrocatalyst, *Natl. Sci. Rev.* 7 (2020) 609–619, <https://doi.org/10.1093/nsr/nwz166>.
- [46] G. Zhu, R. Guo, W. Luo, H.K. Liu, W. Jiang, S.X. Dou, J. Yang, Boron doping-induced interconnected assembly approach for mesoporous silicon oxycarbide architecture, *Natl. Sci. Rev.* 8 (2021) nwaa152, <https://doi.org/10.1093/nsr/nwaa152>.
- [47] J.D. Yi, R. Xie, Z.L. Xie, G.L. Chai, T.F. Liu, R.P. Chen, Y.B. Huang, R. Cao, Highly selective  $\text{CO}_2$  electroreduction to  $\text{CH}_4$  by In situ generated  $\text{Cu}_2\text{O}$  single-type sites on a conductive MOF: stabilizing key intermediates with hydrogen bonding, *Angew. Chem. Int. Ed.* 59 (2020) 23641–23648, <https://doi.org/10.1002/anie.202010601>.
- [48] Y. Gao, Q. Wu, X. Liang, Z. Wang, Z. Zheng, P. Wang, Y. Liu, Y. Dai, M. H. Whangbo, B. Huang,  $\text{Cu}_2\text{O}$  nanoparticles with both {100} and {111} facets for enhancing the selectivity and activity of  $\text{CO}_2$  electroreduction to ethylene, *Adv. Sci.* 7 (2020), 1902820, <https://doi.org/10.1002/advs.201902820>.
- [49] S. Zhu, B. Jiang, W.B. Cai, M. Shao, Direct observation on reaction intermediates and the role of bicarbonate anions in  $\text{CO}_2$  electrochemical reduction reaction on Cu surfaces, *J. Am. Chem. Soc.* 139 (2017) 15664–15667, <https://doi.org/10.1021/jacs.7b10462>.
- [50] Y. Katayama, F. Nattino, L. Giordano, J. Hwang, R.R. Rao, O. Andreussi, N. Marzari, Y. Shao-Horn, An in situ surface-enhanced infrared absorption spectroscopy study of electrochemical  $\text{CO}_2$  reduction: selectivity dependence on surface C-bound and O-bound reaction intermediates, *J. Phys. Chem. C* 123 (2018) 5951–5963, <https://doi.org/10.1021/acs.jpcc.8b09598>.
- [51] N.J. Firet, W.A. Smith, Probing the reaction mechanism of  $\text{CO}_2$  electroreduction over Ag films via operando infrared spectroscopy, *ACS Catal.* 7 (2016) 606–612, <https://doi.org/10.1021/acscatal.6b02382>.
- [52] E. Perez-Gallent, M.C. Figueiredo, F. Calle-Vallejo, M.T. Koper, Spectroscopic observation of a hydrogenated CO dimer intermediate during CO reduction on Cu (100) electrodes, *Angew. Chem. Int. Ed.* 56 (2017) 3621–3624, <https://doi.org/10.1002/anie.201700580>.